Hertlein, Anna; Du Puits, Ronald

Direct measurements of the thermal dissipation rate in turbulent Rayleigh-Bénard convection

Original published in:	Physics of fluids. - [S.l.] : American Institute of Physics. - 33 (2021), 3, art. 035139, 11 pp.
Original published:	2021-02-16
ISSN:	1089-7666
DOI:	10.1063/5.0033746
[*Visited:*	2022-02-23]

Physics of Fluids ARTICLE scitation.org/journal/phf

Direct measurements of the thermal dissipation rate in turbulent Rayleigh–Bénard convection

Cite as: Phys. Fluids 33, 035139 (2021); doi: 10.1063/5.0033746
Submitted: 19 October 2020 · Accepted: 16 February 2021 ·
Published Online: 16 March 2021

Anna Hertlein[a] and Ronald du Puits

AFFILIATIONS

Institute of Thermodynamics and Fluid Mechanics, Technische Universitaet Ilmenau, 98684 Ilmenau, Germany

[a]Author to whom correspondence should be addressed: anna.hertlein@tu-ilmenau.de

ABSTRACT

We report measurements of the thermal dissipation rate in turbulent Rayleigh-Bénard convection using a four-thermistor temperature gradient probe. The measurements have been undertaken in a Rayleigh-Bénard cell filled with air (Prandtl number $Pr = 0.7$). The focus of this work is on large aspect ratios Γ (ratio between the horizontal and vertical extension of the cell), for which reason four datasets in the range of Rayleigh number $Ra = 3.9 \times 10^6$ to $Ra = 1.8 \times 10^9$ were taken at $\Gamma \geq 8$. In order to extend the range toward higher Rayleigh numbers, two smaller aspect ratios were also investigated ($\Gamma = 4$ with $Ra = 1.7 \times 10^{10}$ and $\Gamma = 2$ with $Ra = 1.6 \times 10^{11}$). We present highly resolved, vertical profiles of the thermal dissipation rate in the central vertical axis and discuss how these profiles change with the Rayleigh number. With its maximum near the wall and at the highest Rayleigh number, the thermal dissipation rate decreases monotonically with the distance from the plate. Moreover, the normalized, volume-averaged thermal dissipation rate, which effectively results in the Nusselt number Nu, scales with an exponent of about 0.29 with the Rayleigh number. In the Rayleigh number range investigated here, the dissipation is always higher in the boundary layer than in the bulk region. However, by means of an extrapolation of the considered Rayleigh number range to larger Rayleigh numbers, the intersection point between the dissipation in the boundary layer and the bulk region can be estimated as $Ra \approx 3 \times 10^{12}$.

I. INTRODUCTION

The understanding of the reciprocal transfer between kinetic and thermal energies is very important for the understanding of complex flow fields. The transition from kinetic to thermal energy is called thermal dissipation and can be described by the thermal dissipation rate. We study this quantity by direct measurements in thermal convection.

A very common setup to study thermal convection is the Rayleigh-Bénard setup, where a fluid layer is cooled from above and heated from below. The temperature gradient generates a complex fluid flow, which transports heat from the warm bottom to the cold top plate. This setup is characterized by a set of five dimensionless parameters. The first is the Rayleigh number Ra that describes the thermal force, which drives the flow. As shown in Eq. (1), it depends on the thermal expansion coefficient β, the gravitational acceleration g, the temperature difference ΔT, the distance H between heating and cooling plates, the thermal diffusivity κ, and the kinematic viscosity ν,

$$Ra = \frac{\beta g \Delta T H^3}{\kappa \nu}. \tag{1}$$

The second parameter is the Prandtl number, which is the ratio between the transport coefficients of momentum and heat in the flow field

$$Pr = \frac{\nu}{\kappa}. \tag{2}$$

In this work, we particularly focus on heat transport, which appears between the two horizontal plates. The Nusselt number, which is the third parameter, describes the dimensionless heat flux in response to Ra and Pr. It is defined as the ratio between the convective and the conductive heat flux, $\dot{q}_{convective}$ and $\dot{q}_{conductive}$, respectively,

$$Nu = \frac{\dot{q}_{convective}}{\dot{q}_{conductive}}. \tag{3}$$

Another output parameter is the Reynolds number, which is a typical velocity U of the flow field divided by the molecular velocity ν/H,

$$Re = \frac{U H}{\nu}. \tag{4}$$

In general, Rayleigh–Bénard convection can be considered as a laterally infinite extended, one-dimensional system, in which the mean values of all relevant parameters only change in the vertical direction. Over a long observation time, mean values are constant at each point of any horizontal plane. This is the basis of nearly all concepts concerning heat transport in this system. Many applications, for example, geophysical flows, fulfill this condition fairly well, because the lateral extension is much larger than the vertical. However, the majority of the laboratory experiments and most numerical simulations are conducted in geometries with sidewalls and, hence, do not fully match this theoretical assumption. Usually, a fifth parameter, the aspect ratio Γ, is introduced to describe the ratio of horizontal (diameter d) to vertical (height H) extent,

$$\Gamma = \frac{d}{H}. \tag{5}$$

(For a detailed overview on Rayleigh–Bénard convection see Chillà and Schumacher.[1]) One of the most frequently discussed question in Rayleigh–Bénard convection is the dependence of the dimensionless heat flux in form of the Nusselt number on the Rayleigh and the Prandtl number, which is quite often represented by a scaling law with the scaling exponents γ and γ',

$$Nu \sim Ra^{\gamma} Pr^{\gamma'}. \tag{6}$$

Over the last decades, various scaling laws have been suggested. Under the assumption that heat transport is exclusively set by marginally stable boundary layers, Malkus[2] suggested a scaling exponent of $\gamma = 1/3$ without any Prandtl number dependence. Experiments done by Castaing *et al.*[3] in low-temperature helium near the critical point indicate a smaller exponent, namely, $\gamma = 0.28$. Based on these measurements, Castaing *et al.* developed the so-called mixing-zone model, which is characterized by rising and falling plumes stabilizing the opposite boundary layer. The same scaling law was proposed in a theoretical model of Shraiman and Siggia.[4] They connect the heat flux with the shear in the viscous boundary. With the equations of motion, they derived mathematical expressions for the volume-averaged kinetic and thermal dissipation rates $\langle \varepsilon_u \rangle_V$ and $\langle \varepsilon_{th} \rangle_V$, respectively, and how they are linked with the corresponding dimensionless parameters of Rayleigh-Bénard convection (Nu, Ra, Pr),

$$\langle \varepsilon_u \rangle_V = \frac{\nu^3}{H^4}(Nu - 1) RaPr^{-2}, \tag{7}$$

$$\langle \varepsilon_{th} \rangle_V = \kappa \frac{(\Delta T)^2}{H^2} Nu. \tag{8}$$

In the year 2000, Grossmann and Lohse[5] took up this idea and developed their unifying theory. The basic idea of this work is to correlate the kinetic and the thermal dissipation rates in the boundary layer and the bulk. Later on, they refined the model by replacing the boundary layer and bulk with thermal plumes and turbulent backgrounds.[6] The model predicts four different regimes in the parameter space of Ra and Pr, each of them described by a scaling law with different scaling exponents. The bounds of these regimes in the Ra - Pr phase space are essentially determined by the two-volume averaged dissipation rates $\langle \varepsilon_u \rangle_V$ and $\langle \varepsilon_{th} \rangle_V$. Both quantities are decomposed into a boundary layer and a bulk contribution. Depending on location in the Ra - Pr phase space, either the boundary layer or the bulk fraction of the thermal and the kinetic dissipation rates dominates, respectively. In order to estimate dissipation rates, it is necessary to know, whether the thermal or kinetic boundary layer is larger. This depends on the Prandtl number. For Prandtl numbers below one, the kinetic boundary layer is nested within the thermal boundary layer; for Prandtl numbers above one, it is the other way around. The theoretical model only provides scaling exponents γ and γ' but not the prefactors in Eq. (6). In order to complete the model, the prefactors have to be determined by data either from experiments or from numerical simulations. This is partly difficult since Rayleigh–Bénard experiments and simulations meeting both, a high aspect ratio and a high Rayleigh number, are rare. Therefore, prefactors obtained in aspect ratio $\Gamma = 1$ or $\Gamma = 1/2$ experiments or numerical simulations are currently implemented in the model[7] (see Ahlers *et al.*[8] for a detailed overview).

Even though, dissipation might be a key quantity to understand turbulent convection and to predict the turbulent heat flux, measurements of the thermal dissipation rate are rare. He *et al.*[9] conducted measurements of this quantity in turbulent Rayleigh–Bénard convection with water ($Pr = 7$). The aspect ratios were $\Gamma = 1$ and $\Gamma = 0.5$, respectively. They used probes of different sizes; however, the smallest one was still as large as the thickness of the boundary layer. The authors measured vertical profiles of the thermal dissipation rate and decomposed the quantity into a fraction ε_m which is linked to the mean temperature gradient and another fraction ε_f which is linked to the fluctuations. They found that ε_f predominates in the bulk region, whereas ε_m is the dominant fraction in the boundary layer. Furthermore, they investigated how ε_f and ε_m depend on the Rayleigh number. They found that their contribution scales differently with the Rayleigh number, and they concluded that thermal plumes and the boundary layer must be treated individually.

In a numerical work, Shishkina and Wagner[10] also focused on the separation of the thermal dissipation rate into a plume related fraction and a turbulent background related fraction. Plumes change their shape with varying Rayleigh numbers and form a large-scale circulation at higher Rayleigh numbers. The main result of Shishkina's work is the finding that the contribution of the thermal dissipation rate in the turbulent background related to the whole dissipation increases with the Rayleigh number. Another recent numerical investigation by Bhattacharya *et al.*[11] aims at separating the dissipation field into a boundary layer and a bulk fraction again. In order to gain scaling relations, the authors regarded the dissipation in boundary layer and bulk in a Rayleigh number range from $Ra = 10^6$ to $Ra = 10^8$ and at Prandtl numbers of $Pr = 1$ and $Pr = 100$, respectively. They found that the ratio between the boundary layer and bulk dissipation remains constant over the range of Rayleigh numbers investigated. However, this result is in direct contrast to the Grossmann–Lohse theory, which predicts that this ratio decreases with increasing Rayleigh number.

Our conclusion with respect to the existing data is that thermal dissipation in turbulent convection was exclusively studied in low aspect ratio setups. In general, investigations at a large aspect ratio are very rare, since they require large-scale experiments and/or specific working fluids close to their critical point. Direct numerical simulations become quickly quite complex and expensive as the grid resolution must be higher than in setups with a low aspect ratio. On the other hand, the maximum Rayleigh number in a large aspect ratio cell is much smaller than in a small aspect ratio cell with the same lateral dimension. This is the main reason why experiments[12–15] and

numerical simulations[16–20] are mostly aimed toward aspect ratios of the order of one or even smaller. There are a few papers on flat geometries, but none of them deals directly with thermal dissipation rate. For the sake of completeness, we show some of them below. First, there is a work by another group in Ilmenau, who engaged in an optical measurement technique for examining the velocity field in a flat Rayleigh–Bénard cell[21,22] and the evaluation of a measurement technique to determine the temperature field by means of thermochromic liquid crystals.[23] Furthermore, a few numerical studies at large aspect ratio exist, which mainly focus on turbulent, coherent structures.[24–26] The variation of the aspect ratio involves in that cases a variation of the Rayleigh number.

In our experiment, we measured the thermal dissipation rate highly resolved in space and time in a Rayleigh number range from $Ra = 3.9 \times 10^6$ to $Ra = 1.6 \times 10^{11}$ using a probe with four microthermistors. We run our experiment in a configuration, where the aspect ratio at $\Gamma \geq 8$. The working fluid is air, whose Prandtl number is almost constant $Pr = 0.7$ over the whole temperature range our measurements covered. Measurements of the thermal dissipation rate in this parameter range are unique. We discuss the vertical profiles of the thermal dissipation rate and how they vary with the Rayleigh number. Furthermore, and in analogy to the Grossmann–Lohse theory, we analyze the dissipation in the boundary layer and in the bulk region. This paper is divided as follows: in Sec. II, we describe the Rayleigh–Bénard cell, the construction and the functionality of the new four-thermistor temperature gradient probe and the measurement procedure. In Sec. III, we discuss the results of our measurements and compare them with previous work. We conclude our work in Sec. IV.

II. EXPERIMENTAL SETUP

A. The large-scale Rayleigh–Bénard experiment "Barrel of Ilmenau"

We have undertaken our measurements in a large-scale Rayleigh–Bénard experiment, which is called the "Barrel of Ilmenau." The experiment allows to study thermal convection in a wide range of Rayleigh numbers and aspect ratios. Due to its large size, it also meets the criterion of sufficiently thick boundary layers to probe them with our temperature gradient probe. The test section is filled with air (see Fig. 1). It is of cylindrical shape with an inner diameter of $d = 7.15$ m. The distance between the heated bottom and the cooled top plates is continuously adjustable between $H = 0.2$ m and $H = 6.30$ m. By means of electric heating, we can vary the temperature of the heating plate from $T_{HP} = 20\,^\circ$C to $T_{HP} = 80\,^\circ$C. The cooling system consists of a cooling aggregate and a buffer store, which enables us to adjust the temperature of the cooling plate between $T_{CP} = 10\,^\circ$C and $T_{CP} = 30\,^\circ$C. Nevertheless, the temperature difference should not be larger than $\Delta T = 50$ K, as the cooling power of the cooling aggregate is limited. In order to maintain a constant temperature over the surface of each plate, both plates consist of aluminum with water tubes inside. The temperature of the plates is controlled using multiple thermometers at various locations. The maximum temperature deviation amounts to 0.02 K. An adiabatic sidewall with an active compensation heating system prevents any heat exchange between the inner of the cell and the environment (for more details see du Puits *et al.*[27])

The work presented here mainly focuses on an aspect ratio of $\Gamma = 8$. With a diameter of $d = 7.15$ m, the distance between cooling and heating plates amounts then to $H = 0.9$ m. From our point of view, this is sufficiently large, to exclude any effect of the sidewall on the flow field in middle of the container, where we measure the thermal dissipation rate.[27] With keeping the aspect ratio constant, a range in Rayleigh number from $Ra = 3 \times 10^7$ to $Ra = 3 \times 10^9$ can be set in the test section varying the temperature between $\Delta T = 0.5$ K and $\Delta T = 50.0$ K. However, we consider a total temperature difference of $\Delta T = 3.0$ K as a lower limit for the measurement of the profiles of the thermal dissipation rate ($\Delta T = 2.0$ K for the 2.5 m inset, see below), since even lower temperature gradients would increase the measurement uncertainty. Our setting results in a minimum Rayleigh number for the $d = 7.15$ m diameter test section of $Ra = 1.9 \times 10^8$. In order to extend this range to lower Rayleigh numbers, we inserted a Plexiglas® cylinder with a diameter of $d = 2.50$ m and a height of $H = 0.28$ m. This extends the domain of the Rayleigh number down to $Ra = 3.9 \times 10^6$ with an aspect ratio in the same order ($\Gamma = 9$). In this specific setup with a smaller inset within the larger test section, the boundary condition is perfectly adiabatic. As well the inner of the small inset as the space between the walls of the smaller and the larger test sections represent the same Rayleigh–Bénard flow with equal profiles of the mean temperature in z-direction. Thereby, heat exchange through the wall of the inner cylinder is almost avoided.[28] Since the maximum Rayleigh number in the $\Gamma = 8$ cell is limited by the maximum temperature difference to $Ra = 3 \times 10^9$, but many natural and technical convection problems are characterized by even higher Rayleigh numbers, we did two more measurements at a reduced aspect ratio. One measurement was undertaken at $\Gamma = 4$ and $Ra = 1.7 \times 10^{10}$ and the other one at $\Gamma = 2$ and $Ra = 1.6 \times 10^{11}$. However, one has to consider that the flow in the center of the cell becomes more and more affected by the sidewall. In total, we run six series of measurements of the thermal dissipation rate, whose main parameters are listed in Table I.

Furthermore, during another experimental study, a measurement system at the Barrel of Ilmenau was mounted, which allows to measure the convective wall heat flux $\dot{q}_W$. The definition of the Nusselt number [see Eq. (3)] offers a connection between the Nusselt number and the convective heat flux $\dot{q}_W$,

$$Nu = \frac{\dot{q}_W H}{\lambda \Delta T}. \tag{9}$$

The convective heat flux is measured by heat flux plates of the company Phymeas GbR. They are mounted in the heating and the cooling plates of the Barrel of Ilmenau, respectively. The plates are provided with calibration and a calibration error of 5% is indicated. Further investigations on directly measured Nusselt numbers are planned.

B. The temperature gradient probe

In general, the thermal dissipation rate is defined as $\varepsilon_{th} = \kappa \cdot |\nabla T|^2$. Thus, it is necessary to measure the three-dimensional temperature gradient ∇T. For that, we constructed a multithermistor probe consisting of four single microthermistors with a diameter of about 160 μm and a length of about 340 μm. They are mounted together on a probe with a distance of about $l \approx 2.0$ mm between them. Figure 2 shows photos as well as sketches of the probe. The measured gradients are the ratios between the temperature

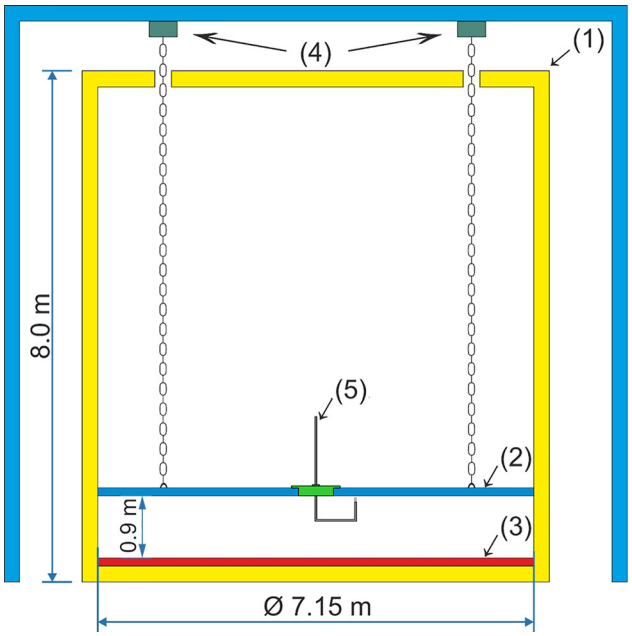

FIG. 1. The setup of the "Barrel of Ilmenau," a very large Rayleigh–Bénard cell with an adiabatic container (1), a cooling plate (2), a heating plate (3), and cranes (4) to lift the cooling plate up and down. In the center of the cooling plate, the temperature gradient probe with its holder (5) is drawn.

difference and the distances between thermistor 1 with the other thermistors 2, 3, and 4,

$$\nabla T = \begin{pmatrix} \frac{T_2 - T_1}{|\vec{l}_{21}|} \\ \frac{T_3 - T_1}{|\vec{l}_{31}|} \\ \frac{T_4 - T_1}{|\vec{l}_{41}|} \end{pmatrix}. \tag{10}$$

In particular, the selection of the appropriate distance between the thermistors was a very complex process, because several points have to be considered. A small distance between the individual thermistors would allow to measure the thermal dissipation rate with a high spatial resolution, which is especially preferable in the boundary layers. Estimating the Kolmogorov length scale $\eta = \left(\nu^3/\langle\varepsilon_u\rangle_V\right)^{1/4}$ (with $\langle\varepsilon_u\rangle_V$ from Grossmann-Lohse theory) shows that the smallest length scales for the considered Rayleigh numbers are in the range $1\,\text{mm} < \eta < 3\,\text{mm}$. However, small distances between the thermistors also result in small differences in the measured temperature. This is not an issue in the boundary layer part. But it increases the measurement uncertainty in the bulk region, where the mean temperature gradient tends to zero. It has to be considered as well that each thermistor affects the fluid flow around. If the distance between them is chosen too small, the measured gradients might be influenced by the interaction of the thermistors with the fluid. He *et al.*[9] investigated the required distances between the sensors very intensively. The size of the thermistors is in the same order of magnitude as those used in this work and the separations between the thermistors are even smaller. With respect to that and since He *et al.* found that l should be smaller than 4 mm, we believe that $l \approx 2\,\text{mm}$ is an appropriate distance. In order to enable measurements of the temperature gradient as close as possible to the surface of the plate, we have chosen a specific arrangement as shown in Fig. 2. Thermistor 1 is located above the other

TABLE I Set of parameters of our measurements with varying Rayleigh number *Ra*, with Γ being the aspect ratio, d the diameter of the cell, H the plate distance, ΔT the temperature difference between the plates, T_{HP} and T_{CP} the plate temperatures of the heating and the cooling plates, T_{bulk} the measured temperature at the midplane, κ the thermal diffusivity, *Nu* the Nusselt number determined by the measurements of the heat flux plates, and δ the thermal boundary layer thickness gained with this Nusselt number with $\delta = H/(2\,Nu)$.

Ra	Γ	d (m)	H (m)	ΔT (K)	T_{HP} (°C)	T_{CP} (°C)	T_{bulk} (°C)	$\kappa\left(\frac{\text{m}^2}{\text{s}}\right)$	Nu	δ (mm)
3.9×10^6	8.9	2.50	0.28	2.0	31.0	29.0	30.0	2.29×10^{-5}	13.0	10.8
1.8×10^7	8.9	2.50	0.28	10.0	35.0	25.0	29.6	2.28×10^{-5}	19.9	7.0
1.9×10^8	7.9	7.15	0.90	3.0	31.5	28.5	30.1	2.29×10^{-5}	38.5	11.7
1.8×10^9	7.9	7.15	0.90	28.9	44.4	15.5	29.9	2.29×10^{-5}	71.8	6.3
1.7×10^{10}	4.0	7.15	1.79	36.0	50.0	14.0	33.3	2.34×10^{-5}	134.0	6.7
1.6×10^{11}	2.0	7.15	3.58	55.0	75.0	20.0	50.2	2.57×10^{-5}	249.7	7.2

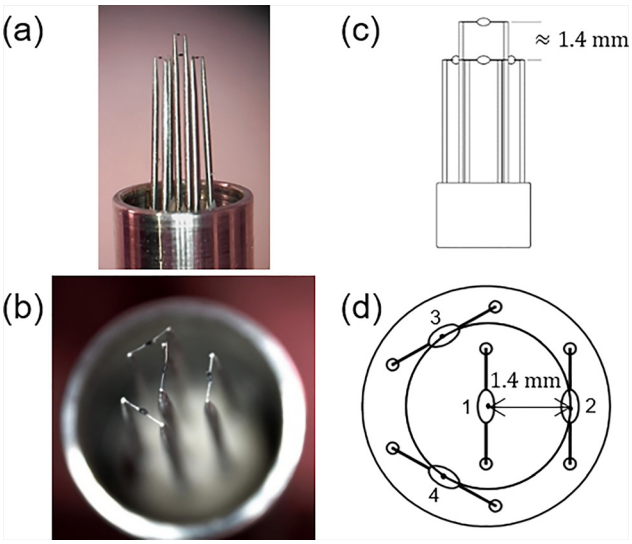

FIG. 2. Photos with side (a) and top views (b) and drawings with side (c) and top views (d) of the multithermistor probe.

sensors. Its center represents the origin of a skew coordinate system, which is formed along with thermistors 2, 3, and 4. With only one sensor as tip of the probe, it is easier to place the probe as close as possible to the cooling plate. Since the coordinate system of the probe is not a Cartesian one and differs from the coordinate system of the test cell, a transformation is necessary to obtain the gradients parallel (x, y) and normal to the wall (z). Our geometrical arrangement of the four thermistors and the specific distances of the thermistors to each other yields a transformation matrix M,

$$M = \begin{pmatrix} 0.7330 & -0.3415 & -0.3349 \\ 0.0000 & -0.5914 & 0.5801 \\ 0.6806 & 0.7317 & 0.7416 \end{pmatrix}. \tag{11}$$

In order to obtain the Cartesian gradients, the measured gradients (s_1, s_2, s_3) has to be multiplied with the matrix M,

$$\begin{pmatrix} x \\ y \\ z \end{pmatrix} = M \cdot \begin{pmatrix} s_1 \\ s_2 \\ s_3 \end{pmatrix}. \tag{12}$$

In addition to the high spatial resolution of our probe, the small-sized microthermistors also allow very fast measurements, which will be important to investigate the dynamics of the thermal dissipation rate (we will do this in a separate paper). The typical response time of the sensors is of the order of 100 ms.[29] We have calibrated the probe with the four thermistors in an isothermal box in the range from 10 °C to 60 °C against a standard platinum thermometer with an uncertainty of ±0.05 K. Since the smallest temperature gradient measured in the bulk region is as low as 4×10^{-3} K/mm at a Rayleigh number of $Ra = 3.9 \times 10^6$ (resulting in a temperature difference of 0.008 K between the thermistors), we decided to improve the accuracy of our measurements by an additional *in situ* calibration. This is done in the center of the test section, where the mean temperature gradient is the smallest. To this aim, we defined the temperature of thermistor 3 as the reference value [see Eq. (13)]. Then, we determined correction values $\xi_{1,2,3,4}$ as the difference between the mean values of the single sensors $\langle T\rangle_{t,1,2,3,4}|_{z=H/2}$ in the cell center (at $z = H/2$) and the reference temperature gained from Eq. (13). These correction values [see Eq. (14)] are added to the respective temperature signals of the whole measurement series [see Eq. (15)]. With that, corrections in the typical order of 0.1 K were made,

$$\langle T\rangle_{t,3}|_{z=H/2} \stackrel{!}{=} T_{ref}\,, \tag{13}$$

$$\xi_{1,2,3,4} = \left(\langle T\rangle_{t,1,2,3,4}|_{z=H/2} - T_{ref}\right), \tag{14}$$

$$T_{1,2,3,4} = T_{1,2,3,4,meas} + \xi_{1,2,3,4}. \tag{15}$$

Another kind of measurement uncertainty is how precisely we know the distance between the individual sensors. The shapes of the thermistors are irregular and the positioning during the bonding process is not perfect. Thus, we validate the vertical distance between thermistors 2, 3, and 4 and thermistor 1, respectively, by correlating the measured profiles of the mean temperatures $\langle T\rangle_{t,1}(z)$ with $\langle T\rangle_{t,2}(z)$, $\langle T\rangle_{t,3}(z)$, and $\langle T\rangle_{t,4}(z)$. Since the temperature field $\langle T\rangle_t(z)$ is the same for all four microthermistors, we can determine the vertical distance between the thermistors by shifting the profiles $\langle T\rangle_{t,2}(z)$, $\langle T\rangle_{t,3}(z)$, and $\langle T\rangle_{t,4}(z)$ in such a way that all four profiles collapse. The shift is coincident with the vertical distances between the sensors. Unfortunately, this method can not be applied for the horizontal distances, for which reason we use the construction distances.

C. Measurement setup and procedure

The multithermistor probe is connected to an L-shaped rectangular, hollow brass rod, which is installed on a positioning system standing on top of the cooling plate. The rod enters the measuring volume through a cylindrical hole in the cooling plate closed by a cap. In order to prevent heat losses but to guarantee that the rod is guided well defined, we used a Teflon® lead with a rectangular duct for the brass rod (see Fig. 3).

An interesting aspect of our measurements is the orientation of the probe with respect to the global recirculation in the test section. In order to find the latter one, we made the recirculation visible using smoke. Unlike in the well-studied aspect-ratio-one cells, in which the vector of the global recirculation fluctuates around a fixed plane, our experiments in the aspect-ratio-eight cell show a completely irregular behavior of the global recirculation vector at the measurement position below the center of the cooling plate including all angles between 0 and 360°.[30] Furthermore, the knowledge of former LDA measurements gives information about the local velocity vector.[31] If the vector of flow is from the L-shaped rod to the thermistors, this might be a source of error in certain flow states, but most of the time, it does not disturb the measurement significantly. A positioning system at the upper side of the cooling plate moves the rod in the vertical direction. Its positioning accuracy is better than ±10 μm. We find the zero position of the probe by moving it toward the cooling plate until thermistor 1 gets in contact with the plate surface. This contact can be identified by a characteristic sequence in the measurement signal.

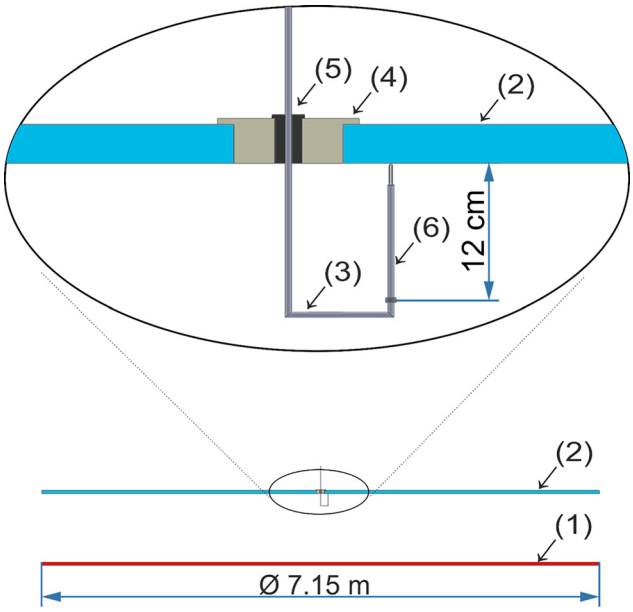

FIG. 3. Sketch of the installation of the multithermistor probe with connector (6) with the heating plate (1), the cooling plate (2), the brass rod (3), closing cap (4), and the Teflon® lead (5).

From this position, we move the probe down by 10 μm and set this as the z-position at which our measurement starts. Taken into account the size of the sensors and the geometry of the probe, this position corresponds to a distance $z_0 = 0.8$ mm (see Fig. 4).

In order to measure the profile of the thermal dissipation rate $\varepsilon_{th}(z)$, we distribute the measurement points in a logarithmic manner. This means that the distance between two points is comparatively small close to the cold top plate and gets larger toward the midplane. We also increase the time of the measurements at each position. This is necessary, since the fluctuations of the individual derivatives $\nabla_x T$, $\nabla_y T$, and $\nabla_z T$ increase with increasing distance to the plate and the uncertainty of the statistical values would rise. In order to prevent this, we prolonged the measuring times at those z-positions where higher standard deviations are estimated. With that, we could keep the confidence interval in a band of 0.07 K (before it was 0.2 K). All measurements were undertaken with a rate of 200 samples per second, which

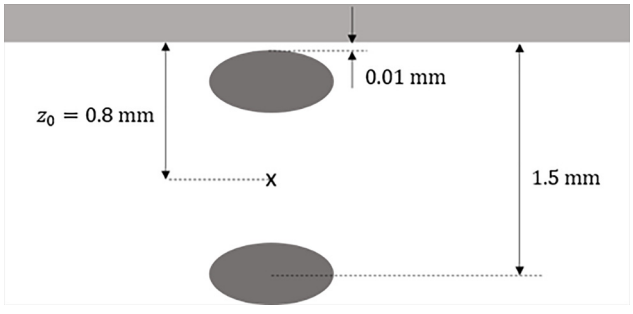

FIG. 4. Sketch of the location of the multithermistor probe relative to the cooling plate in order to determine the first measuring point of the profile.

is appropriate, as the Kolmogorov time scale $\tau = \left(\nu/\langle\varepsilon_u\rangle_V\right)^{1/2}$ is in the range of $0.075\,\mathrm{s} < \tau < 0.49\,\mathrm{s}$ in the considered parameter range. Each sensor of the multithermistor probe is connected to a measuring bridge and a preamplifier for signal conditioning. The bridge works with an extremely low measurement current of $I_{Th} = 5\,\mu$A and the maximum temperature increase in the microthermistors by self-heating remains less than 10 mK. Subsequently, the signal is amplified and noise is removed by a low-pass filter with a cutoff frequency of 10 Hz. This value corresponds to the response time of the microthermistors. From the output of the bridge, the signal enters a PC-based data acquisition system with a resolution of 24 bit. Using the calibration curve, the temperature is calculated and the data are stored on a hard disk.

III. RESULTS AND DISCUSSION

A. Profiles of the mean thermal dissipation rate

We start our discussion with two profiles of the mean thermal dissipation rate $\langle\varepsilon_{th}\rangle_t(z)$ we measured near the cooling plate at Rayleigh numbers $Ra = 1.9 \times 10^8$ and $Ra = 1.8 \times 10^9$. The results are directly comparable, because we varied the Rayleigh number in these two cases only by changing the temperature difference from $\Delta T = 3$ K ($Ra = 1.9 \times 10^8$) to $\Delta T = 28.9$ K ($Ra = 1.8 \times 10^9$). The aspect ratio and the cell height were kept constant, namely, at $\Gamma = 8$ and $H = 0.9$ m.

In Fig. 5, we show the mean values of the thermal dissipation rate $\langle\varepsilon_{th}\rangle_t(z)$ as function of the distance z from the cooling plate normalized by the height H of the cell. In order to assign measurement values to both, the boundary layer and the bulk, respectively, we indicate the boundary layer thicknesses calculated from the measured Nusselt numbers with $\delta = H/(2\,Nu)$ by the dashed lines. These quantities amount to $\delta_\circ = 11.7$ mm for the smaller and $\delta_\square = 6.3$ mm for the larger Rayleigh number. For both cases, we found the measured mean thermal dissipation rate to be larger in the boundary layer and to become smaller toward the midplane. Furthermore, we indicate the global volume averaged mean $\langle\varepsilon_{th}\rangle_V$ that we obtained from Eq. (8). For this theoretically determined quantity we used the Nusselt numbers provided by the Grossmann–Lohse theory[32] with using the evaluated system of equations by Stevens *et al.*[7] While the values of the local dissipation rate lie above this value close to the wall, they fall below it toward the midplane. The crossovers of the profiles with the values from Eq. (8) move toward the wall with increasing Rayleigh number. In our specific cases, the profiles cross at $z_{V,\circ} = 94.3$ mm ($z_{V,\circ}/H = 0.01$) at $Ra = 1.9 \times 10^8$ and $z_{V,\square} = 40.0$ mm ($z_{V,\square}/H = 0.04$) at $Ra = 1.8 \times 10^9$, indicated by the vertical dashed–dotted lines.

In order to study the thermal dissipation at Rayleigh numbers smaller height of $H = 0.28$ m between the heating and the cooling plates of the facility. The aspect ratio amounts to $\Gamma = 9$, which is slightly higher than in the $d = 7.15$ m cell, but we could set up experiments down to a Rayleigh number of $Ra = 3.9 \times 10^6$. Since the height of the two cells is not the same, the results gained in the two cells are not directly comparable with respect to the Rayleigh number, since the thermal dissipation rate varies with the height (or the temperature difference), even if the Rayleigh number is kept constant. Nevertheless, the smaller cell offers the same shapes of curves and the variation of the intersection point between the measured profiles and theoretical values also shifts toward the wall if the Rayleigh number increases. In our specific cases at $Ra = 3.9 \times 10^6$ ($\delta = 10.7$ mm) and

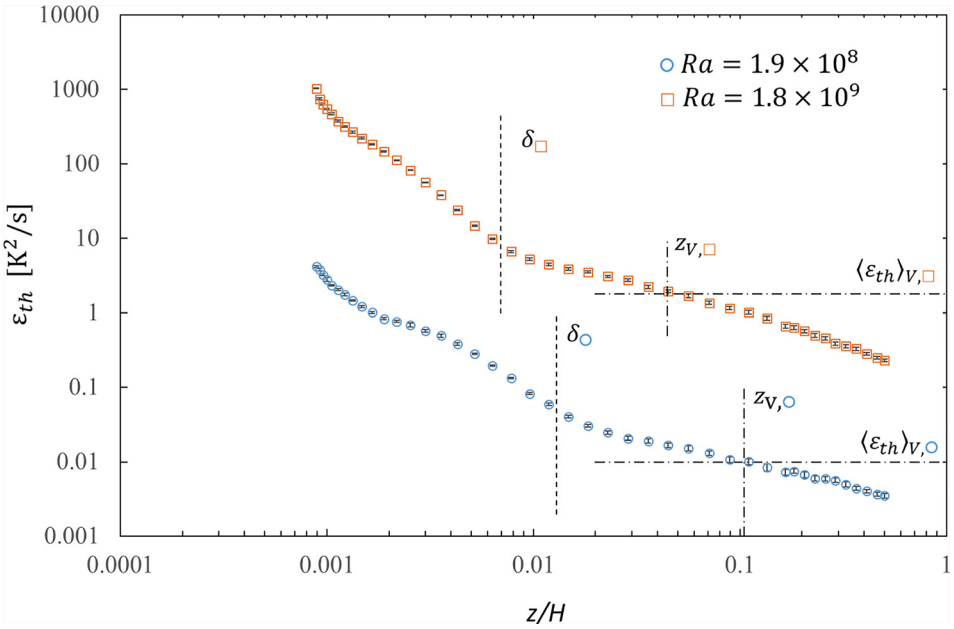

FIG. 5. Profiles of the mean thermal dissipation rate $\varepsilon_{th}(z/H)$ at the cooling plate at aspect ratio $\Gamma = 8$ and two different Rayleigh numbers $Ra = 1.9 \times 10^8$ and $Ra = 1.8 \times 10^9$. The distance z is normalized by the height of the cell H. The horizontal, dashed–dotted lines show the theoretical volume and time-averaged thermal dissipation rates $\langle\varepsilon_{th}\rangle_{V,\circ}$ and $\langle\varepsilon_{th}\rangle_{V,\square}$, the vertical, dashed lines the respective boundary layer thicknesses $\delta_\circ$ and $\delta_\square$, and the vertical, dashed–dotted lines the intersection points $z_{V,\circ}$ and $z_{V,\square}$ between the measured profile and the predictions from Eq. (8). The error bars indicate the 95% confidence bounds and are in an order from 1.1% to 6.8%.

$Ra = 1.8 \times 10^7$ ($\delta = 6.3$ mm), the intersection point changes from $z = 17.1$ mm to $z = 9.4$ mm. The reader finds a list of data in Table II.

B. Normalized profiles of all six Rayleigh numbers

In order to compare the profiles of the mean dissipation rate $\langle\varepsilon_{th}\rangle_t$ measured at different cell heights and temperature differences, we introduce $\tilde{\varepsilon}_{th} = \langle\varepsilon_{th}\rangle_t / \left(\kappa(\Delta T/H)^2\right)$ and plot the results in Fig. 6. The distance from the wall z is normalized by the thickness of the boundary layer δ. With increasing Rayleigh number, $\tilde{\varepsilon}_{th}$ increases continuously. The typical trend with a maximum close to the plate surface and a minimum at the cell center virtually coincides with all considered Rayleigh numbers. In all cases, it is seen that the decrease in the thermal dissipation rate is steeper in the boundary layer than in the bulk region.

In the next step, we validate our measurements by computing time and volume-averaged thermal dissipation rate $\langle\varepsilon_{th}\rangle_{V,meas}$ of the measured profiles and we compare these values with those from Eq. (8). We assume (i) the mean dissipation rate is constant over the horizontal extent (at sufficiently large aspect ratio) and (ii) a symmetry of the lower half and the upper half of the Rayleigh–Bénard cell. With these assumptions, we form the integral over the profiles of the thermal dissipation rate from the surface of the cooling plate at $z = 0$ to the midheight of the cell at $z = H/2$,

$$\langle\varepsilon_{th}\rangle_{V,meas} = \frac{2}{H}\int_{z=0}^{\frac{H}{2}} \langle\varepsilon_{th}\rangle_t(z)dz. \tag{16}$$

Due to the finite size of the sensors (see Fig. 2), it is not possible to measure the dissipation rate closer to the surface of the cooling plate as $z = 0.8$ mm (see Fig. 4). This problem concerns all considered cell configurations. At some specific configurations, there is also a lack of data toward the midheight of the cell. This appears if either the plate distance is very large (the holder of the probe cannot be made arbitrary long) or the plate distance is too small (the L-shaped holder touches the surface of the heating plate, see Fig. 3). For the general case, therefore, the integral according to Eq. (17) consists of three terms and looks as follows:

TABLE II. Selected results of the measurements dependent on the Rayleigh number *Ra*: δ– boundary layer thickness, $\langle\varepsilon_{th}\rangle_V$– theoretical time and volume-averaged thermal dissipation rate, z_{GL} – intersection point between the measured profiles and $\langle\varepsilon_{th}\rangle_V$, $\varepsilon_{th}(z = \delta/5)$, $\varepsilon_{th}(z = \delta)$, $\varepsilon_{th}(z = H/2)$– mean thermal dissipation rates at $z = \delta/5$, $z = \delta$, and $z = H/2$.

Ra	δ (mm)	$\langle\varepsilon_{th}\rangle_V$ (K²/s)	z_V (mm)	$\varepsilon_{th}(z = \delta/5)$ (K²/s)	$\varepsilon_{th}(z = \delta)$ (K²/s)	$\varepsilon_{th}(z = H/2)$ (K²/s)
3.9×10^6	10.70	0.01	17.1	3.51×10^{-1}	3.13×10^{-2}	2.34×10^{-3}
1.8×10^7	7.03	0.58	9.4	1.90×10^{1}	1.10×10^{0}	9.60×10^{-1}
1.9×10^8	11.69	0.01	94.4	6.62×10^{-1}	5.37×10^{-2}	3.50×10^{-3}
1.8×10^9	6.26	1.80	40.0	2.49×10^{2}	9.29×10^{0}	2.31×10^{-1}
1.7×10^{10}	6.68	1.44	129.8	4.56×10^{2}	1.82×10^{1}	1.79×10^{-1}
1.6×10^{11}	7.17	1.11	177.4	6.74×10^{2}	2.84×10^{1}	6.56×10^{-2}

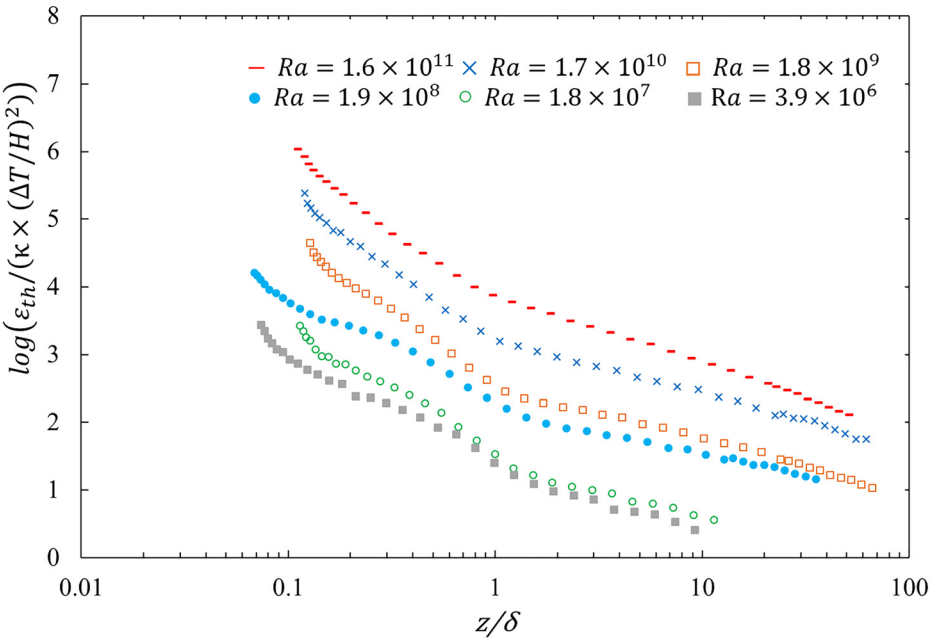

FIG. 6. Profiles of normalized thermal dissipation rate $\tilde{\varepsilon}_{th}$ with $\tilde{\varepsilon}_{th} = \langle \varepsilon_{th} \rangle_t / (\kappa (\Delta T/H)^2)$. The z-position is normalized by the thermal boundary layer thickness δ.

$$\varepsilon_{th\,V,meas} = 2/H \left(\underbrace{\left(\int_{z=0}^{z=0.8} \varepsilon_{th}(z)dz \right)}_{\text{estimated}} + \underbrace{\left(\int_{z=0.8}^{z=z_1} \varepsilon_{th}(z)dz \right)}_{\text{measured}} + \underbrace{\left(\int_{z=z_1}^{z=H/2} \varepsilon_{th}(z)dz \right)}_{\text{estimated}} \right). \tag{17}$$

In order to estimate the near-wall term, we use the measurement of the wall heat flux $\dot{q}_W$ that provides the gradient of the mean temperature normal to the wall. With the assumption that the horizontal components of the three-dimensional temperature gradient $\partial T/\partial x$ and $\partial T/\partial y$ are negligibly very close to the wall with respect to the wall normal component $\partial T/\partial z$, the thermal dissipation rate can be estimated from $\partial T/\partial z$. The Fourier law delivers the temperature gradient $\partial T/\partial z$,

$$\frac{\partial T}{\partial z} = \frac{\dot{q}}{\lambda}. \tag{18}$$

In this case, we used the measured heat flux $\dot{q}_W$, which was measured with the heat flux measurements described in Sec. II A. The near-wall thermal dissipation rate is then estimated as

$$\varepsilon_{th,wall} = \kappa \left(\frac{\partial T}{\partial z} \right)^2. \tag{19}$$

The area between the wall and the first measurement point at $z = 0.8$ mm is linear interpolated. For the estimation of the dissipation rate near the midplane of the cell, we used the last measured points of the profiles to interpolate an algebraic power law in the form $\varepsilon_{th,bulk} = C z^{\alpha}$. Table III shows the detailed numbers.

In Fig. 7, we plot the volume-averaged dissipation rates $\langle \varepsilon_{th} \rangle_{V,meas}$ vs the Rayleigh number. The plot covers the results at $\Gamma \geq 8$ (filled circles) as well as $\Gamma = 4$ and $\Gamma = 2$ (empty circles). All measured values are normalized by $\kappa (\Delta T/H)^2$, which eventually leads to the Nusselt number $(\langle \tilde{\varepsilon}_{th} \rangle_{V,meas} = (\langle \varepsilon_{th} \rangle_{V,meas})/(\kappa (\Delta T/H)^2) = Nu)$. As expected, $\langle \tilde{\varepsilon}_{th} \rangle_{V,meas}$ increases with the Rayleigh number. The dashed line shows a linear slope that corresponds scale to a power law with an exponent of $\beta = 0.29$. Despite an obvious scatter of the measurement points, the rise is comparable to the rise of the linear slope of the data points in the log/log-plot. For comparison, we also plot the correspondent theoretical value $\langle \varepsilon_{th} \rangle_V$.[32] Our measurements do not fully coincide with the prediction by the Grossmann–Lohse theory, but there are various reasons for the difference. The first reason is the fact that our measurements are presently limited to the central axis of the experiment $(x, y = 0)$.

We assume homogeneity of the dissipation rate over x, y planes for infinite long time, but this assumption might not be true for the time interval we measured. Another reason could be the different aspect ratio. While our measurements were undertaken at $\Gamma \geq 8$, the Nusselt numbers provided from the theory are based on experiments/simulations at aspect ratio one and smaller.

TABLE III. Prefactors C and scaling exponents α of the interpolation function to estimate the profiles down to $z = H/2$ for all respective Rayleigh numbers Ra.

Ra	C	α
3.6×10^6	1.5×10^{-1}	-0.8
1.9×10^7	5.5×10^0	-0.9
1.7×10^{10}	2.7×10^2	-1.4
1.6×10^{11}	3.1×10^2	-1.2

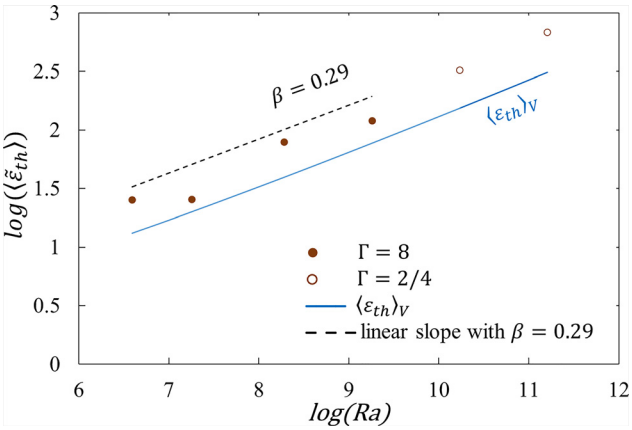

FIG. 7. Thermal dissipation rate $\langle\tilde{\varepsilon}_{th}\rangle_{V,meas}$ averaged in time and space from experiments (red circles) dependent on the Rayleigh number. The dashed black line represents a linear slope with an exponent $\beta = 0.29$. The blue line shows the curve of the theoretical values determined with Eq. (8). For this theoretical consideration, the Nusselt number provided by the Grossmann–Lohse theory was used.

C. Dependence of the dissipation on the Rayleigh number

One of the core ideas of the Grossmann-Lohse theory is that the ratio of the dissipation in the boundary layer and the bulk varies with the Rayleigh number (and the Prandtl number as well). In this subsection, we discuss the measured dissipation in the boundary layer and the bulk region, respectively. Like Bhattacharya *et al.*,[11] we calculate the dissipation as the integral of the thermal dissipation rate over the volumes of the boundary layer and the bulk. Then, we can write the dissipation D_{bl} in the boundary layer and D_{bulk} in the bulk as follows:

$$D_{bl} = 2\,\frac{\pi}{4}d^2\int_{z=0}^{z=\delta}\langle\varepsilon_{th}\rangle_t(z)dz\,, \tag{20}$$

$$D_{bulk} = 2\,\frac{\pi}{4}d^2\int_{z=\delta}^{\frac{H}{2}}\langle\varepsilon_{th}\rangle_t(z)dz. \tag{21}$$

We again normalize the dissipation $\tilde{D} = (DH^2)/(\kappa\Delta T^2)$ to make the measurements comparable at the various configurations. The results are shown in Fig. 8. Considering only the results at high aspect ratio $\Gamma \geq 8$, the normalized dissipation monotonically increases with the Rayleigh number in both, the boundary layer and the bulk region. As usual for the Nusselt number, we also fit power laws of the form

$$\tilde{D} \sim Ra^{\varphi}. \tag{22}$$

We compute the scaling exponents by incorporating only the measurements at $\Gamma = 9$ and $\Gamma = 8$ ($Ra = 3.9 \times 10^6$ to $Ra = 1.9 \times 10^9$). While the thermal dissipation scales with $\varphi_{bl} = 0.21$ in the boundary layer part, the resulting exponent in the bulk region is $\varphi_{bulk} = 0.30$. Our results are consistent with the predictions of the Grossmann–Lohse theory, where a change of the dominance of the dissipation from the boundary layer to the bulk region is predicted, if the Rayleigh number is sufficiently high. The theory provides this transitional Rayleigh number as high as $Ra_{trans} = 1.4 \times 10^{11}$ for a Prandtl number of $Pr = 0.7$. The interpolation of our two fits intersects at $Ra \approx 3 \times 10^{12}$, which is not far from the predicted value. In contrast to this, recent direct numerical simulations by Bhattacharya[11] do not coincide with our measurements. The authors also examined the ratio of the dissipation within the boundary layer and the bulk. They found the ratio of both contributions $\tilde{D}_{bl}/\tilde{D}_{bulk}$ to be almost constant if the Rayleigh number is changed. Although we do not have an explanation, the aspect ratio might play a role in this discrepancy. We see such an effect in our measurements considering the trend of the dissipation at $\Gamma = 4$ and $\Gamma = 2$ (see Fig. 8). Although the Rayleigh number is higher

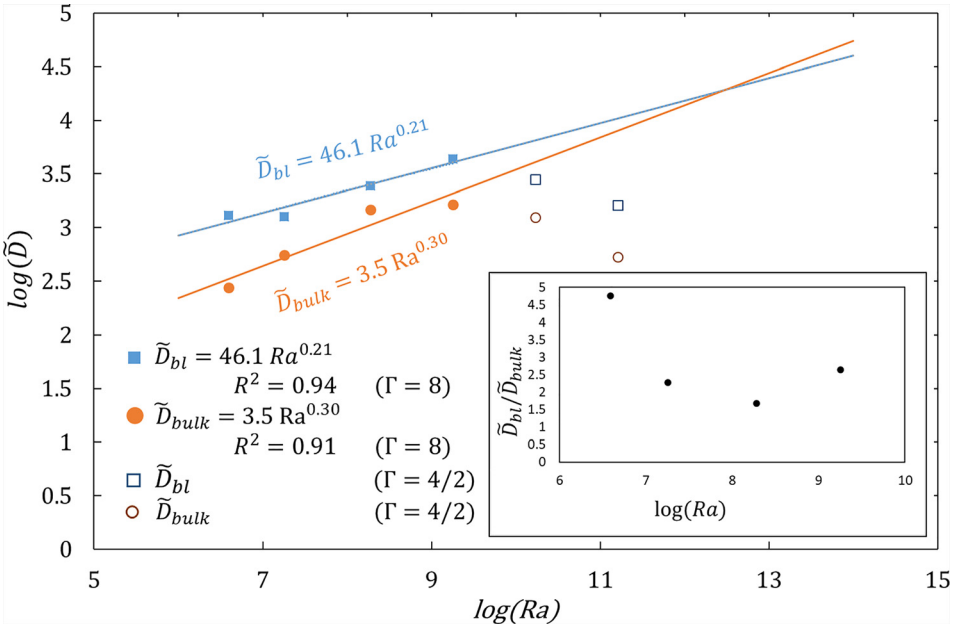

FIG. 8. Normalized dissipation $\tilde{D} = (DH^2)/(\kappa\Delta T^2)$ vs Rayleigh number. R^2 are the coefficients of determination. In the inset, the ratio between $\tilde{D}_{bl}$ and $\tilde{D}_{bulk}$ is shown.

than in all $\Gamma \geq 8$ measurements, the ratio $\tilde{D}_{bl}/\tilde{D}_{bulk}$ becomes larger again, if the aspect ratio gets smaller.

IV. CONCLUSION

Finally, we summarize the results of our experimental investigations of thermal dissipation in turbulent Rayleigh–Bénard convection at a large aspect ratio $\Gamma \geq 8$. By means of a unique four-thermistor temperature gradient probe, we measured the instantaneous 3d-gradient field of the temperature along the central (vertical) axis of a large-scale Rayleigh–Bénard cell called "Barrel of Ilmenau." From these highly time and space resolved measurements, we compute the thermal dissipation rate. We have executed our measurements at six different Rayleigh numbers $3.9 \times 10^6 < Ra < 1.6 \times 10^{11}$ at a Prandtl number $Pr = 0.7$, whereas for the two highest Rayleigh numbers $Ra = 1.7 \times 10^{10}$ and $Ra = 1.6 \times 10^{11}$, the aspect ratios were $\Gamma = 4$ and $\Gamma = 2$, respectively. At all considered Rayleigh numbers, the values of the thermal dissipation rate are always larger and the curve shapes are steeper in the boundary layer than in the bulk region. The integration of the dissipation rates over the volumes of the boundary layer and the bulk shows that dissipation dominates in the boundary layer in the considered Rayleigh and Prandtl number ranges. In both regions, the dissipation increases with the Rayleigh number, but the trend is steeper in the bulk region. We found (by interpolation) that the dissipation in the bulk region would become dominant over the dissipation in the boundary layer at a Rayleigh number of $Ra = 3 \times 10^{12}$. The normalized average of the thermal dissipation rate over the whole measurement section reveals the Nusselt number. The exponent of the relation is of the order of 0.29. This is quite close to other measurements that show exponents slightly smaller or larger than 0.3.[3,33–35] However, there is some deviation from the Grossmann-Lohse theory. The reason might be the large aspect ratio we did our measurements in, but also some kind of inhomogeneity of the experimental results in the horizontal direction (we measure only at a single position with respect to each horizontal plane). For this reason, measurements in the side areas of the cell seem to be reasonable in the future that may validate our results. Furthermore, it would make sense to design an even smaller temperature gradient probe to get better access into the temperature field very close to the wall.

ACKNOWLEDGMENTS

The authors wish to acknowledge the support from the German Research Foundation under the Grant No. PU 436/11–1. Moreover, we thank Sabine Scherge and Vigimantas Mitschunas for the technical assistance to run the experiment and Gerrit Kampers from University of Oldenburg for the construction of the multithermisor probe.

DATA AVAILABILITY

The data that support the findings of this study are available from the corresponding author upon reasonable request.

REFERENCES

[1]F. Chillà and J. Schumacher, "New perspectives in turbulent Rayleigh-Bénard convection," Eur. Phys. J. E **35**(7), 58 (2012).
[2]W. V. R. Malkus, "Discrete transitions in turbulent convection," Proc. R. Soc. London, Ser. A **225**, 185 (1954).
[3]B. Castaing, G. Gunaratne, F. Heslot, L. Kadanoff, A. Libchaber, S. Thomae, X.-Z. Wu, S. Zaleski, and G. Zanetti, "Scaling of hard thermal turbulence in Rayleigh-Bénard convection," J. Fluid Mech. **204**, 1 (1989).
[4]B. I. Shraiman and E. D. Siggia, "Heat transport in high-Rayleigh-number convection," Phys. Rev. A **42**(6), 3650 (1990).
[5]S. Grossman and D. Lohse, "Scaling in thermal convection: A unifying theory," J. Fluid Mech. **407**, 27 (2000).
[6]S. Grossmann and D. Lohse, "Fluctuations in turbulent Rayleigh–Bénard convection: The role of plumes," Phys. Fluids **16**(12), 4462 (2004).
[7]R. J. A. M. Stevens, E. P. van der Poel, S. Grossmann, and D. Lohse, "The unifying theory of scaling in thermal convection: The updated prefactors," J. Fluid Mech. **730**, 295 (2013).
[8]G. Ahlers, S. Grossmann, and D. Lohse, "Heat transfer and large scale dynamics in turbulent Rayleigh-Bénard convection," Rev. Mod. Phys. **81**(2), 503 (2009).
[9]X. He and P. Tong, "Measurements of the thermal dissipation field in turbulent Rayleigh-Bénard convection," Phys. Rev. E **79**, 26306 (2009).
[10]O. Shishkina and C. Wagner, "Analysis of thermal dissipation rates based on direct numerical and large–eddy simulations of turbulent Rayleigh -Bénard convection," in *Progress in Turbulence II*, edited by M. Oberlack, G. Khujadze, S. Günther, T. Weller, M. Frewer, J. Peinke, and S. Barth (Springer Berlin Heidelberg, Berlin, Heidelberg, 2007), p. 201.
[11]S. Bhattacharya, R. Samtaney, and M. K. Verma, "Scaling and spatial intermittency of thermal dissipation in turbulent convection," Phys. Fluids **31**, 75104 (2019).
[12]X. L. Qiu and P. Tong, "Onset of coherent oscillations in turbulent Rayleigh-Bénard convection," Phys. Rev. Lett. **87**, 094501 (2001).
[13]X. He, D. Funfschilling, H. Nobach, E. Bodenschatz, and G. Ahlers, "Transition to the ultimate state of turbulent Rayleigh-Bénard convection," Phys. Rev. Lett. **108**(2), 024502 (2012).
[14]P. Urban, T. Králík, P. Hanzelka, V. Musilová, T. Vězník, D. Schmoranzer, and L. Skrbek, "Thermal radiation in Rayleigh-Bénard convection experiments," Phys. Rev. E **101**(4), 043106 (2020).
[15]V. Musilová, T. Králík, M. L. Mantia, M. Macek, P. Urban, and L. Skrbek, "Reynolds number scaling in cryogenic turbulent Rayleigh–Bénard convection in a cylindrical aspect ratio one cell," J. Fluid Mech. **832**, 721 (2017).
[16]M. S. Emran and J. Schumacher, "Conditional statistics of thermal dissipation rate in turbulent Rayleigh-Bénard convection," Eur. Phys. J. E **35**(10), 108 (2012).
[17]S. Wagner and O. Shishkina, "Aspect-ratio dependency of Rayleigh-Bénard convection in box-shaped containers," Phys. Fluids **25**(8), 85110 (2013).
[18]Y. Zhang, Q. Zhou, and C. Sun, "Statistics of kinetic and thermal energy dissipation rates in two-dimensional turbulent Rayleigh–Bénard convection," J. Fluid Mech. **814**, 165 (2017).
[19]A. Xu, L. Shi, and H.-D. Xi, "Statistics of temperature and thermal energy dissipation rate in low-Prandtl number turbulent thermal convection," Phys. Fluids **31**(12), 125101 (2019).
[20]D.-L. Dong, B.-F. Wang, Y.-H. Dong, Y.-X. Huang, N. Jiang, Y.-L. Liu, Z.-M. Lu, X. Qiu, Z.-Q. Tang, and Q. Thou, "Influence of spatial arrangements of roughness elements on turbulent Rayleigh-Bénard convection," Phys. Fluids **32**, 45114 (2020).
[21]C. Kästner, C. Resagk, J. Westphalen, M. Junghähnel, C. Cierpka, and J. Schumacher, "Assessment of horizontal velocity fields in square thermal convection cells with large aspect ratio," Exp. Fluids **59**, 171 (2018).
[22]C. Cierpka, C. Kästner, C. Resagk, and J. Schumacher, "On the challenges for reliable measurements of convection in large aspect ratio Rayleigh-Bénard cells in air and sulfur-hexafluoride," Exp. Therm. Fluid Sci. **109**, 109841 (2019).
[23]S. Moller, C. Resagk, and C. Cierpka, "On the application of neural networks for temperature field measurements using thermochromic liquid crystals," Exp. Fluids **61**, 111 (2020).
[24]A. Pandey, J. D. Scheel, and J. Schumacher, "Turbulent superstructures in Rayleigh-Bénard convection," Nat. Commun. **9**, 2118 (2018).
[25]R. J. A. M. Stevens, A. Blass, X. Zhu, R. Verzicco, and D. Lohse, "Turbulent thermal superstructures in Rayleigh-Bénard convection," Phys. Rev. Fluids **3**, 041501 (2018).
[26]D. Krug, D. Lohse, and R. J. A. M. Stevens, "Coherence of temperature and velocity superstructures in turbulent Rayleigh–Bénard flow," J. Fluid Mech. **887**, A2 (2020).

[27]R. Du Puits, C. Resagk, and A. Thess, "Thermal boundary layers in turbulent Rayleigh–Bénard convection at aspect ratios between 1 and 9," New J. Phys. **15**, 013040 (2013).
[28]L. Li, N. Shi, R. Du Puits, C. Resagk, J. Schumacher, and A. Thess, "Boundary layer analysis in turbulent Rayleigh-Bénard convection in air: Experiment versus simulation," Phys. Rev. E **86**, 026315 (2012).
[29]R. Du Puits, A. Loesch, J. Salort, and F. Chillà, "Thermal boundary layers in turbulent Rayleigh-Bénard convection with rough surfaces," arXiv:1710.06206v2 (2017).
[30]A. Lösch, private communication (1/2020).
[31]R. Du Puits, C. Resagk, and A. Thess, "Structure of viscous boundary layers in turbulent Rayleigh-Bénard convection," Phys. Rev. E **80**, 036318 (2009).
[32]S. Grossmann and D. Lohse, "Prandtl and Rayleigh number dependence of the Reynolds number in turbulent thermal convection," Phys. Rev. E **66**, 016305 (2002).
[33]P. Urban, P. Hanzelka, V. Musilová, T. Králík, M. L. Mantia, A. Srnka, and L. Skrbek, "Heat transfer in cryogenic helium gas by turbulent Rayleigh–Bénard convection in a cylindrical cell of aspect ratio 1," New J. Phys. **16**(5), 053042 (2014).
[34]J. J. Niemela and K. R. Sreenivasan, "Confined turbulent convection," J. Fluid Mech. **481**, 355 (2003).
[35]P.-E. Roche, B. Castaing, B. Chabaud, and B. Hébral, "Heat transfer in turbulent Rayleigh–Bénard convection below the ultimate regime," J. Low. Temp. Phys. **134**, 1011 (2004).